






Anomalous Hall conductivity control in Mn₃NiN antiperovskite by epitaxial strain along the kagome plane

D. Torres-Amaris ^{1,*}, A. Bautista-Hernandez ², Rafael González-Hernández ³,
Aldo H. Romero ^{4,5,2} and A. C. Garcia-Castro ^{1,†}

¹*School of Physics, Universidad Industrial de Santander, Carrera 27 Calle 09, Bucaramanga 680002, Colombia*

²*Facultad de Ingeniería, Benemérita Universidad Autónoma de Puebla, Apartado Postal J-39, Puebla, Pue. 72570, México*

³*Departamento de Física y Geociencias, Universidad del Norte, Km. 5 Vía Antigua Puerto Colombia, Barranquilla 080020, Colombia*

⁴*Department of Physics and Astronomy, West Virginia University, Morgantown, West Virginia 26506-6315, USA*

⁵*Department of Physics and Materials Science, University of Luxembourg, 1511 Luxembourg, Luxembourg*



(Received 8 April 2022; revised 21 October 2022; accepted 21 October 2022; published 7 November 2022)

Antiferromagnetic manganese-based nitride antiperovskites, such as Mn₃NiN, hold a triangular frustrated magnetic ordering, thanks to their kagome lattice formed by the Mn atoms along the (111) plane. As such, the magnetic frustration imposes a nontrivial interplay between the symmetric and asymmetric magnetic interactions, which can only reach equilibrium in a noncollinear magnetic configuration. Consequently, the associated electronic interactions and their possible tuning by external constraints, such as applied epitaxial strain, play a crucial role in defining the microscopic and macroscopic properties of such topological condensed matter systems. In this paper, we explored and explained the effect of the epitaxial strain imposed within the (111) plane, in which the magnetic and crystallographic symmetry operations are kept fixed, and only the magnitude of the ionic and electronic interactions are tuned. We found a tangible enhancement in the anomalous Hall conductivity along the (111) plane ($\sigma_{111}^{\text{AHE}}$) for compression values, whereas, for tension, the AHC is dramatically reduced. As such, the $\sigma_{111}^{\text{AHE}}$ component fetches a maximum increase of 26%, with respect to the unstrained structure, for a compression value close to -1.5% . Our findings indicate a distinct correlation between the anomalous Hall conductivity and the Berry curvature along the (111) plane as a function of the strain. Here, the nondivergent Berry curvature acts as the source and the strain as the control mechanism of this anomalous transport phenomenon.

DOI: [10.1103/PhysRevB.106.195113](https://doi.org/10.1103/PhysRevB.106.195113)

I. INTRODUCTION

Antiperovskites, A_3BX [1] (also known as inverse-perovskites) such as Mn₃NiN, are cubic structures similar to perovskites in which the cation and anion position are interchanged within the unit cell for the standard perovskite crystal structure. Thus, the anions occupy the octahedral center instead of the corners, which becomes the site for the transition metal cations, forming a XA_6 octahedra. This type of coordination, coupled with their magnetic response, gives unique properties such as the anomalous Hall conductivity, AHC [2,3], negative thermal expansion [4], giant piezomagnetism [5], magnetic frustration [6,7], among others [8–19]. In particular, the magnetic frustration in triangular magnetic coordination relies on the Mn–Mn exchange and the Mn–N–Mn superexchange interaction. Thus, the metallic RKKY interaction, which favors an antiferromagnetic collinear arrangement [20], is more prominent but is in competition with the superexchange [21,22] interaction mediated by the nitrogen at the cell center. Apart from the exchange and the superexchange, there is also an antisymmetric coupling, the Dzyaloshinskii-Moriya interaction, DMI, which is present in

the (111) plane inducing canting, which further increases the frustration [7,23]. Combining all the discussed interactions converges into nontrivial, noncollinear, and possibly chiral magnetic ordering. In this case, the chirality is of vectorial nature and comes from the removal of the mirror symmetry due to the magnetic orderings, developing a well-defined handedness given by $k = \frac{2}{3\sqrt{3}} \sum_{ij} [\vec{S}_i \times \vec{S}_j]$ (where i, j runs over all the magnetic moments) [24,25]. For example, the triangular frustrated magnetism in Mn₃NiN is compatible with the Γ_{5g} and Γ_{4g} [6] magnetic orderings. The Γ_{4g} (MSG. 166.101) ordering is symmetric under the simultaneous application of both the time-reversal symmetry \mathcal{T} , and the mirror symmetry \mathcal{M} , along the M_{100} , M_{110} , and M_{010} planes in the Seitz notation; conversely, in the Γ_{5g} (MSG. 166.97) ordering, the $\mathcal{T} * \mathcal{M}$ is broken [3]. Moreover, although the overall electronic band structures of both magnetic phases are fairly similar, the mirror symmetry breaking in the Γ_{4g} allows a sizable AHC, unlike in the case of Γ_{5g} in which the AHC is null [3]. The AHE in antiferromagnets has risen in research interest due to the possibility of dissipation-less current [26] thanks to the large AHC found in Mn₃Sn and Mn₃Ge [27–29]. Despite presenting a low density of states at the Fermi level, noncollinear antiferromagnetic antiperovskites are good conductors with a tunable AHC, with the strain as the key to accessing this controllability. The strong magnetostructural

*daniel.torres@saber.uis.edu.co

†acgarcia@uis.edu.co

coupling present in the Mn-based antiperovskites [30,31], on top of the subtle balance between the magnetic, ionic, and electronic structure, opens the door to engineering a route for AHC controlling using external constraints. Although several studies had already been commented on the potential controllability of the AHC in Mn_3NiN by other authors [2,3,32,33], the source of its behavior is not yet completely understood. For example, the reported AHC calculations for Mn_3NiN range from $\sigma_{111} = -301 \text{ S cm}^{-1}$ [34] to $\sigma_{111} = 525 \text{ S cm}^{-1}$ [35] (see Table SI in Supplemental Material [36]), a very wide range likely related to a strong dependence on the calculations approach and parameters chosen by the authors. Remarkably, the AHC in (001) Mn_3NiN strained thin films has been reported as $\sigma_{xy} \approx 170 \text{ S cm}^{-1}$ based-on theoretical calculations whereas the experimentally measured value in the same work is around $\sigma_{xy} = 22 \text{ S cm}^{-1}$ [2]. Despite the disagreement, when the measured and computed AHC are compared, their conclusion was related to a direct compression (tension) to increase (decrease) relation between the strain and the AHC. However, applying the strain in such a direction would distort the crystal into a tetragonal symmetry, changing the magnetic and structural relationship and adding a weak-ferromagnetic canting into the magnetic response [5]. Because the symmetry is the trigger of the AHC in the antiferromagnetic antiperovskites, distortions, and changes in symmetry operations could put a veil over the actual control mechanism and physical origins of this property in Mn_3NiN . Moreover, the experimental epitaxial growth of thin films of antiperovskites onto perovskites, SrTiO_3 , has been achieved [37,38] demonstrating the feasibility of obtaining strained thin-films. Another experimental study was performed, achieving an epitaxial growth of Mn_3NiN on the piezoelectric BaTiO_3 [39] showing a correlation between the strain and the AHC values. So far, it is possible to experimentally explore the effect of the strain on antiferromagnetic nitride antiperovskites such as Mn_3GaN and Mn_3NiN . Notwithstanding these efforts, the explanation of the strain effect, its link with the electronic and ionic structure in this material, and the origin of a possible experimental control of the AHC by means of the strain, still allows room for a more profound comprehension. Therefore, in this paper, we show from first-principles calculations the analysis of the epitaxial strain as a control parameter of the electronic properties. Furthermore, we explored the AHC, and the Berry curvature BC features in the antiferromagnetic antiperovskite Mn_3NiN as a prototype among its family. Thus, our results explain the physical origin of the AHC controllability and possible experimental tuning.

This paper is organized as follows: We present the computational details and theoretical approaches required for the analysis of structural and electronic phenomena within the Mn_3NiN antiperovskite (in Sec. II). Then, we condensed our results and research associated with the structure behavior, electronic properties, anomalous Hall conductivity, and the Berry curvature (in Sec. III). Finally, we provide our conclusions, in Sec. IV, and general remarks.

II. COMPUTATIONAL DETAILS

We performed first-principles calculations within the density-functional theory (DFT) [40,41] approach by us-

ing the VASP code (version 5.4.4) [42,43]. The projected-augmented waves scheme, PAW [44], was employed to represent the valence and core electrons. The electronic configurations considered in the pseudopotentials, as valence electrons, are Mn ($3p^6 3d^5 4s^2$, version 02Aug2007), Ni ($3p^6 3d^8 4s^2$, version 06Sep2000), and N ($2s^2 2p^3$, version 08Apr2002). The exchange-correlation was represented within the generalized gradient approximation GGA-PBEsol parametrization [45]. The Mn:3d orbitals were corrected through the DFT+ U approximation within the Liechtenstein formalism [46]. Due to the strong magnetostructural response observed in the Mn_3AN antiperovskites [47], we used the $U = 2.0 \text{ eV}$ parameter in the Mn:3d orbitals. This U value allows the structural optimization to reproduce the experimentally observed lattice parameter, which is key in obtaining an appropriate charge distribution and, ultimately, the electronic properties under strain. Moreover, we also compared the PBEsol+ U obtained electronic structure of Mn_3NiN with the computed by the strongly constrained and appropriately normed semilocal density functional, SCAN, [48,49], observing a fair agreement of the electronic structure in both cases. Importantly, recent reports of SCAN-based calculations have shown results in good agreement with the experimental reports, including lattice constant [50,51], the magnetic and the electronic structure [30] in strongly-correlated 3d perovskites and Heusler Mn-based alloys [52]. All the procedures described above are essential due to the needed accuracy related to the lattice degrees of freedom as a function of the applied strain and its effect on the magnetostructural behavior. The periodic solution of the crystal was represented by using Bloch states with a Monkhorst-Pack [53] k -point mesh of $12 \times 12 \times 12$ and 600 eV energy cut-off to give forces convergence of less than $0.001 \text{ eV \AA}^{-1}$ and an error in the energy less than 10^{-6} eV . The spin-orbit coupling (SOC) was included to consider noncollinear magnetic configurations [54]. The anomalous Hall conductivity, and associated observables, were obtained with the Python library WANNIERRB [55] using the maximally localized Wannier functions and the tight-binding Hamiltonian generated with the WANNIER90 package [56]. The interpolation was performed with 80 Wannier functions with projections on the s , p , d orbitals for the Mn and Ni atoms and s , p for N atoms. For the disentanglement process, we used an energy window +3.0 eV higher than Fermi level as the maximum, and none for the minimum, and a convergence tolerance of $5.0 \times 10^{-8} \text{ \AA}^2$. We obtained, with the support of the WannierTools code [57], the number of band crossings around the Fermi energy, for the range between -1.3 to 1.3 eV , as well as their position in energy and momentum. The latter considering a energy-gap crossing (E_w) below the threshold of $E_w = 0.050 \text{ eV}$ computed in a $17 \times 17 \times 17$ k mesh. The atomic structure figures were elaborated with the VESTA code [58]. Finally, the band structure was analyzed with the Python library PYPROCAR [59].

III. RESULTS AND DISCUSSION

As commented before, we aim to avoid additional contributions induced by the strain application in the (001) plane of the 5-atom reference, depicted in Fig. 1(a). Therefore, we studied the effect of the epitaxial strain applied only in the directions

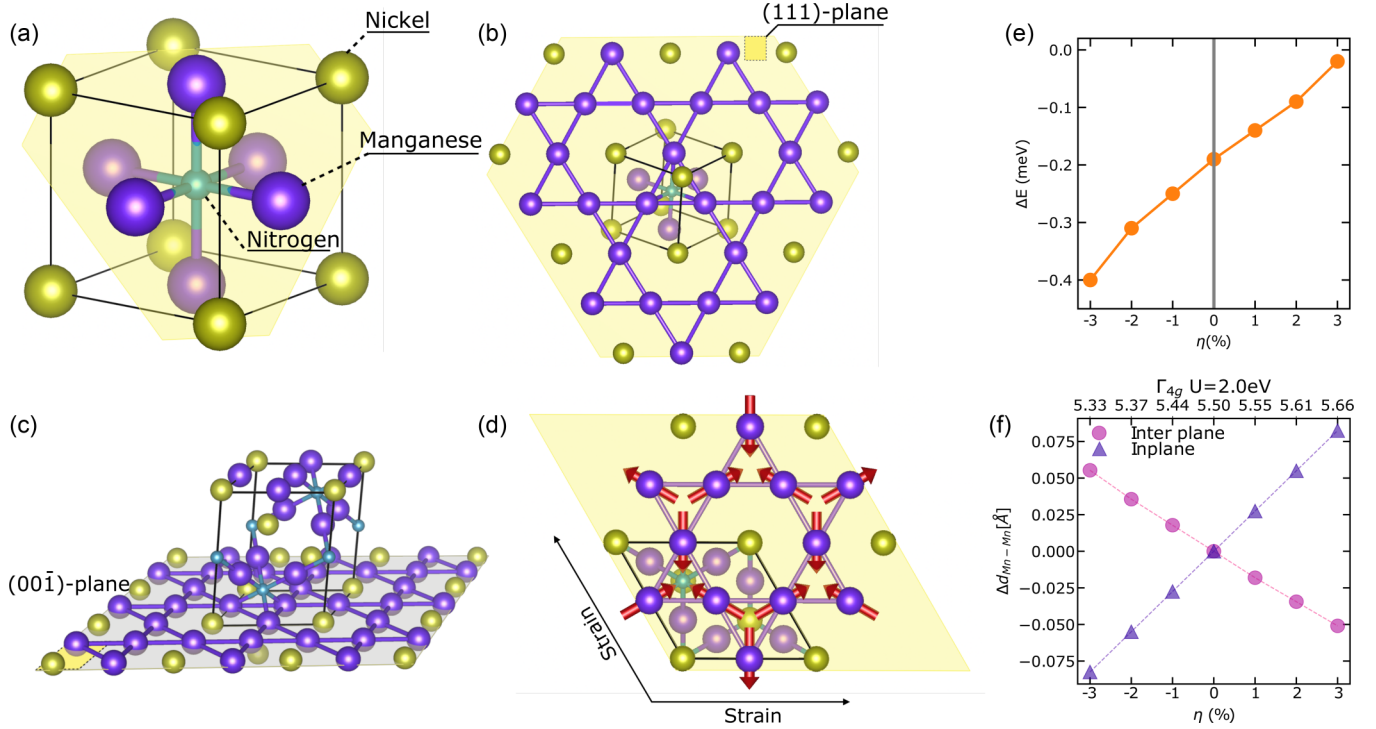


FIG. 1. (a) Mn_3NiN cubic structure showing the Mn, Ni, and N atoms in violet, yellow, and green colors, respectively. Here, the (111) plane is shown in yellow color. (b) The kagome lattice, on the (111) plane formed by the Mn atoms, is highlighted on top of the cubic Mn_3NiN structure. (c) 15-atom hexagonal reference obtained after rotating the 5-atom structure, aligning the (111) plane kagome lattice with the xy plane. (d) Noncollinear antiferromagnetic Γ_{4g} ordering, in which the magnetic moments per atom are depicted in red color. Additionally, the kagome lattice is also shown, as well as the schematics of the strain application. (e) Ground state energy difference, $\Delta E = E_{\Gamma_{4g}} - E_{\Gamma_{5g}}$, vs the applied epitaxial strain suggesting a lower energy for the Γ_{4g} in each case. (f) Variation of the interplane and in-plane Mn–Mn distances as a function of the epitaxial strain.

parallel to the (111) plane so that the kagome lattice, magnetic ordering, and their associated symmetry conditions are conserved. To observe the atomic arrangement present in the (111) plane and its spatial orientation, a broader view of that zone is shown in Fig. 1(b). Here, the kagome lattice formed by the Mn atoms is highlighted in a yellow plane. To gain access to the (111) plane of the 5-atom reference, the structure was rotated to make that plane parallel to the cartesian xy plane as shown in Fig. 1(c). In such orientation, it is obtained an equivalent 15-atom hexagonal cell shown in the same figure. This achieves a better representation of the structural symmetry and allows the homogenous application of the epitaxial strain. In this new representation, the a direction of the lattice belongs in the xy plane and serves as a linearly independent crystallographic direction to apply the epitaxial strain. As it can be seen in Fig. 1(d), stretching along the plane would only change the Mn–Mn distance and not the atomic arrangement. In this setup, the strain controls the intensity of the exchange and the superexchange interactions only by modifying the interatomic distances but conserving the magnetic symmetry.

Concretely, the strain was applied as follows. The a lattice parameter is varied along with the values from -3% to $+3\%$. This still allows the full relaxation of the crystal structure and atomic positions along the c direction in all cases. The applied strain percentage η is defined in terms of

the unstrained lattice parameter a_0 and the imposed value a as

$$\eta = \frac{a - a_0}{a_0} \times 100\%, \quad (1)$$

As such, the above relationship, Eq. (1), gives compression and tension over the structure for negative and positive values of η , respectively.

Since the electronic, magnetic, and crystalline structures of Mn_3NiN are strongly entangled due to its sizable magnetostructural coupling, the cell optimization and electronic relaxation were carefully performed within the PBEsol + U approximation. The latter in order to reproduce the experimental unstrained cell lattice constant ($a_0 = 3.886$ Å below $T_N = 262$ K) [60] with a stable Γ_{4g} magnetic ordering and to obtain a correct relaxed structure under strain. The best agreement between the experiment measured and the computed lattice parameter was found for $U = 2.0$ eV (see Table SII in the Supplemental Material [36]). This correction leads to a hexagonal cell with the parameters of $a = 5.496$ Å and $c = 6.726$ Å within the stable Γ_{4g} magnetic ordering. This value of lattice parameters are equivalent to a lattice parameter $a_0 = 3.885$ Å in the 5-atom reference. Therefore, the Hubbard correction and the volume cell optimization helped to avoid a prestrained setup, which is the case of pure LDA/PBE based calculations, in which a volume adjustment is needed because of the under/overestimation of the

experimentally observed value [51]. Moreover, recent studies indicate a strong dependence on the electronic and lattice degrees of freedom in Mn-based compounds [30,49]. The structural stability of the Γ_{4g} phase of Mn_3NiN was tested under epitaxial strain by obtaining the full phonon-dispersion curves at $\eta = -3.0\%$, 0.0% , and $+3\%$, see Fig. S1(a) in the Supplemental Material [36]. The latter aims to ensure that the ranges of strain chosen were within the limits of the structural stability and that no phase transitions might be induced. As shown in Fig. S1(a) in the Supplemental Material [36], the full phonon-dispersion shows no imaginary or unstable phonons, confirming the structural and vibrational stability of Mn_3NiN under the considered strain values. Furthermore, the magnetic phase stability of the Γ_{4g} over the Γ_{5g} was also tested [see Fig. 1(e)]. As it can be observed from this figure, the compression epitaxial strain reinforces and stabilizes the Γ_{4g} order, whereas, for expansion strain values, the difference in energy between the antiferromagnetic orderings is reduced. Thus, the negative strain values serve as a mechanism to freeze in the Γ_{4g} ordering in the Mn_3NiN . In the Mn_3NiN case, both magnetic orderings would present similar magnetocrystalline anisotropy energy (MAE) in the absence of strain, corroborated experimentally [61–63] and indicating a possible combination of the Γ_{4g} and Γ_{5g} orderings in the experimentally synthesized samples. Nonetheless, a more recent report points to a bias of the magnetism in Mn_3NiN towards the Γ_{4g} ordering [34] and, in agreement with our results in Fig. 1(e), the Γ_{4g} ordering is more stable with respect to the Γ_{5g} state, at compressive strain values. Moreover, we have also explored the possible presence of a ferromagnetic canting along the (111) axis. Nevertheless, such canting vanishes after full atomic and electronic relaxation under strain. The latter can be explained in terms of the lattice dynamics of the Mn_3NiN antiperovskites, which shows that the FM state along the (111) axis is dynamically unstable, inducing an unstable phonon at the R point related to out-of-phase octahedral rotations [49]

The variations of the plane-to-plane distance between the kagome planes, in comparison with the distance between two Mn nearest atoms of the same plane, are presented in Fig. 1(f). The compression (tension) strain application, directly on the plane of the magnetic kagome lattice, produces the expected response of increasing (decreasing) the separation of the (111) family of planes, as shown in the graph of Fig. 1(f). Furthermore, linear variations of the distance between Mn atoms of the same plane induced inverse linear variation in separating the kagome planes. Consequently, the exchange and superexchange interactions can be finely tuned, ultimately gaining control over the frustration mechanism. Thus, the (111) applied strain is advantageous from the symmetry point of view because the initial $R\bar{3}m$ symmetry is preserved along the deformation path on the 15-atom reference. Therefore, the symmetry relationships do not change; instead, only the electronic effects can be tuned through the control over the interacting moments by the epitaxial strain. Additionally, symmetry preservation allows straining and optimizing on the 15-atom reference and then returning to the 5-atom representation to perform the rest of the calculations and analysis, avoiding electronic bands unfolding issues. To recover the 5-atom representation, we made use of the transformation matrices, as implemented in the FINDSYM tool [64,65]. In what

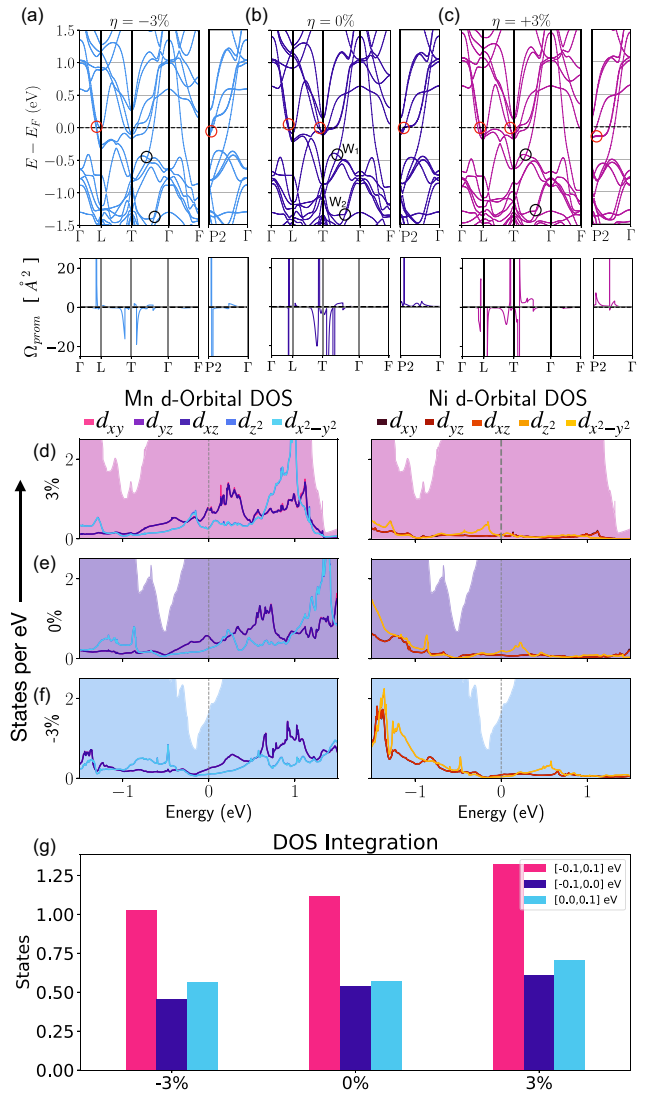


FIG. 2. [(a)–(c)] Electronic band structure (first row) and Berry curvature (second row) of the Mn_3NiN in the Γ_{4g} noncollinear magnetic phase. Here, marked in a black circles are presented two Weyl nodes in the $\text{T}-\Gamma$ path as well as various nontopological band crossings in red circles close to the Fermi level. [(d)–(f)] Density of states, DOS, for the -3.0% , 0.0% , and $+3.0\%$ strain values including the d orbitally projected Mn and Ni states. (g) DOS states integration for an energy range of 0.1 eV under, over, and around the Fermi energy.

follows, all the calculations and analyses are carried out on the 5-atom reference for each relaxed strained cell.

The electronic band structure and the Berry curvature calculated along the $\Gamma-L-T-\Gamma-F$, and $P2-\Gamma$ paths in the BZ for the $\eta = -3.0\%$, 0.0% , and $+3.0\%$ in the 5-atom reference are presented in Figs. 2(a)–2(c) with a relevant Weyl node near Fermi in the $\text{T}-\Gamma$ path marked inside a red circle. Here, the $\text{L}-\text{T}$ path lies along the (111) plane (where the kagome lattice lies) while the $\text{P2}-\Gamma$ path runs perpendicularly to the same plane. When the structure is compressed, the energy bands close to the Fermi energy in the $\text{L}-\text{T}$ path are pushed away from the Fermi level [see Fig. 2(a)]. Meanwhile, as shown in the same figure, electron bands shift up in energy together in

the P2– Γ path. On the other hand, the behavior is the opposite when tension is applied, as observed in the $\eta = +3\%$ case presented in Fig. 2(c). The Berry curvature, in the second row of the Figs. 2(a)–2(c), shows a distinctive behavior in the L–T path; all the remaining path show very localized and discontinuous Berry curvature while in the mentioned path the curvature is a smooth and spread function. The extracted projections, per atomic specie, of the electronic band structure for $\eta = -3.0\%$, 0.0% , and 3.0% (see Fig. S2 in the Supplemental Material [36]) show that Mn : $3d$ states represent the major contribution above the Fermi level. Meanwhile, Ni : $3d$ states dominate the band structure under the Fermi energy, with its most substantial contribution around -1.25 eV. Both Mn and Ni atomic species share the intermediate ($-0.5, +0.5$) eV range of energy. Thus, the conduction phenomena result from the hybridization of the Mn and Ni d orbitals around the Fermi energy. Aiming to analyze the available charge and states around the Fermi level, we computed the DOS for $\eta = -3\%$, 0% , and $+3\%$ and the results are contained in Figs. 2(d)–2(f). Here, we observed a displacement of the total DOS with respect to the energy as a response to the applied strain. Tracking the minimum of the DOS, located at -0.5 eV in the $\eta = 0.0\%$ DOS plot in Fig. 2(e), which moves up (down) in energy for compression (tension), this behavior becomes clear. More precisely, the available states near the Fermi level decrease with compression and increase with tension, see Fig. 2(g). To further dive into the DOS subtleties around the Fermi level, the Mn and Ni : $3d$ orbitals projections of the DOS are included in Figs. 2(d)–2(f). As it can be observed, the contribution at the Fermi level from the $3d_{xy/yz/xz}$ orbitals increase (decrease) for tension (compression) strain values. The same is the case for $3d_{z^2/x^2-y^2}$. In general, the $3d$ orbitals are pushed upwards in energy when the structure is compressed. In the case of Ni: $3d$ orbitals, a marginal contribution is observed close to the Fermi level. Finally, the direct integration of the total DOS for each η in the $[-0.1, +0.1]$ eV interval, as presented in Fig. 2(g), confirms the relationship between the electronic states and the strain inferred from the complete and partial DOS analysis. Moreover, the integration of the DOS over the ranges $[-0.1, 0.0]$ and $[0.0, +0.1]$ eV for the occupied and unoccupied bands, respectively, follow the same behavior already observed in the $[-0.1, +0.1]$ eV interval.

Before discussing our AHC findings, it is worth mentioning the different sources behind the AHC. The AHC in crystals can be the result of different sources: the intrinsic, side jump, and the skew scattering contribution, as shown in Ref. [66]. The last two of them are a consequence of impurities in the crystal that deflect and scatter the electrons sideways. In this paper, we concentrate our attention on the intrinsic component of the AHC, which results from the electronic, magnetic, and structural properties of a perfect crystal. Additionally, the intricate combination of the many interactions present in the frustrated triangular shape created between the Mn atoms in the kagome plane reduces the symmetry to $R\bar{3}m$ in the Γ_{5g} case. Finally, in the case of the Γ_{4g} magnetic ordering, shown in Fig. 1(e), the \mathcal{M} symmetry is also removed, ending up with the $R\bar{3}m'$ symmetry. This lack of \mathcal{M} -symmetry is essential for the existence of AHC in the Γ_{4g} phase. The \mathcal{M} symmetry is also the reason for the absence

of that property in the Γ_{5g} phase. Thus, the AHC reported in this work is calculated based on the relationship defined as follows [66]:

$$\sigma_{\alpha\beta}^{\text{AHC}} = -\frac{e^2}{\hbar} \epsilon_{\alpha\beta\gamma} \int_{\text{BZ}} \sum_n \frac{d^3\vec{k}}{(2\pi)^3} f_n(\vec{k}) \Omega_n^\gamma(\vec{k}). \quad (2)$$

The latter, Eq. (2), as implemented in the WANNIERRB code [55]. Here, in Eq. (2), $\epsilon_{\alpha\beta\gamma}$ is the antisymmetric tensor, $\sum_n f_n(\vec{k}) \Omega_n^\gamma(\vec{k})$ is the summation over all the included bands contribution to the Berry curvature $\Omega_\gamma(\vec{k})$, and $f_n(\vec{k})$ is the Fermi distribution. In Eq. (2), the γ subscript runs over a discrete grid of energy points, allowing the AHC calculation in other energy levels apart from the Fermi level. By looking at the Eq. (2), two main factors are candidates to explain the AHC behavior as a function of the epitaxial strain: The available electronic states around the Fermi level and the Berry curvature integration in the BZ. The Γ_{4g} phase of the Mn_3NiN system is a noncollinear antiferromagnet with a nonzero magnetic moment of each Mn atom but with zero net magnetization. Consequently, without a net internal or external magnetic field, the Hall conductivity must result from the anomalous Hall effect (AHE) through a nonvanishing Berry curvature, as in Eq. (2). The latter is resulting in the following tensor for the $R\bar{3}m'$ magnetic symmetry group [3,67]:

$$\sigma_{\Gamma_{4g}} = \begin{pmatrix} 0 & \sigma_{xy} & -\sigma_{xy} \\ -\sigma_{xy} & 0 & \sigma_{xy} \\ \sigma_{xy} & -\sigma_{xy} & 0 \end{pmatrix} \quad (3)$$

with all the nonzero components identical $\sigma_{xy} = \sigma_{zx} = \sigma_{yz}$ and therefore represented all by the σ_{xy} component. The strain application proposed in this paper is now advantageous because the symmetry preservation guarantees a fixed AHC tensor form and symmetry conditions, as seen in Eq. (3). As such, the setup for the strain, as seen in Fig. 1(e), is the key to studying the AHC in Mn_3NiN as a pure function of the strain without altering the allowed symmetry features, and then, the variations on the AHC in the (111) plane $\sigma_{111}^\eta = \frac{1}{\sqrt{3}}(\sigma_{xy}^\eta + \sigma_{yz}^\eta + \sigma_{zx}^\eta)$ can be extracted as a function of η in the kagome lattices.

Figure 3(a) shows the σ_{111} component of the AHC as a function of the energy, in the energy range $[-0.5, +0.5]$ eV, for strain values between $\eta = -3.0\%$ to 3.0% . In Fig. 3(b), is presented a bar plot condensing the σ_{111} value at the Fermi level for each strain value, as well as their error bars. The latter error bars, marked in red in Fig. 3(a), were estimated as the standard deviation of the last 20 adaptive refinement iterations [55] while computing the σ_{xy} component based on the Eq. (2). Interestingly, the AHC results show a particular behavior; its value does not just increase or decrease with the epitaxial strain; as seen in Fig. 3(a), the whole function suffers a flattening with the compressive and tensile stress incremental. Additionally, the maxima and minima of the conductivity function diverge away from the Fermi level with both types of deformation. Furthermore, as seen in the barplot of Fig. 3(b), the tensile strain produces almost an AHC vanishing value, stretching the (111) plane as low as $\eta = +1\%$ and upwards reduces the conductivity dramatically. The compression, on the other hand, induces an increase of the AHC

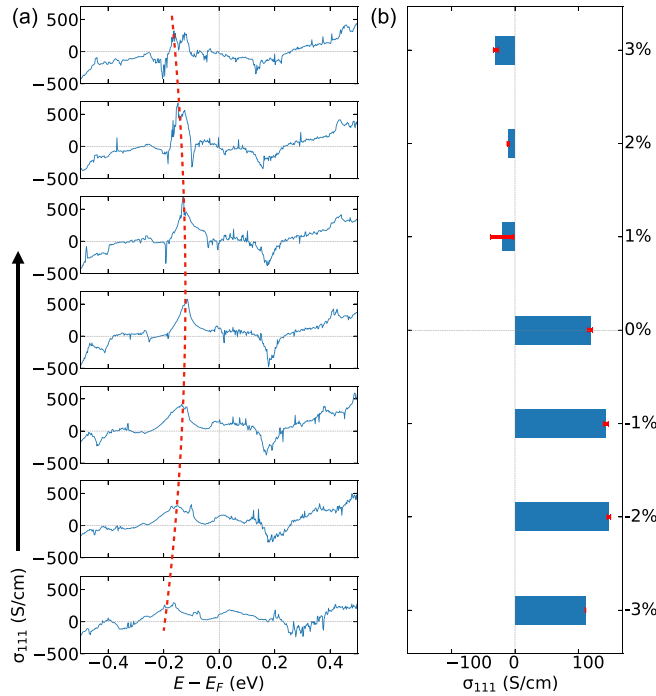


FIG. 3. (a) Anomalous Hall conductivity as a function of energy for various strain values. The AHC around -0.2 eV is showing a downward shifting behavior marked with a red dashed line for compression and tension strain values alike. (b) AHC value extracted at Fermi energy, including the error estimated as the standard deviation of the last 20 computational iterations.

from $\sigma_{111}^{0\%} = 114 \text{ S cm}^{-1}$ to $\sigma_{111}^{-1\%} = 144 \text{ S cm}^{-1}$ representing an increase of 26%. However, the AHC remains constant in a plateau zone that holds until $\eta = -2\%$. Further values of strain compression, after $\eta = -2\%$, does not enhances the AHC, instead, the conductivity drops after this strain value, reaching $\sigma_{111}^{-3\%} = 111 \text{ S cm}^{-1}$ for $\eta = -3\%$, a value similar to the case $\eta = 0\%$. Looking at Fig. 3(a), a small spike of AHC is spotted just under the Fermi level for $\eta = 0.0\%$. Later, it disappears for tension but enhances under compression, growing nonstop along the interval $0\% \geq \eta \geq -2.0\%$. Moreover, the mentioned spike moves up to energies higher than the Fermi level, being its maximum synchronized with the Fermi level for a compressive η between -1.0% and -2.0% . Thus, our findings suggest that the area under the AHC curve is redistributed with the strain rather than shifted. Considering the Eq. (2) and aiming for gathering more information on the origin of the AHC control mechanism, the $\sigma_{111}^{-1.5\%}$ and the Berry curvature were calculated. The conductivity for the additional strain value turned out as $\sigma_{111}^{-1.5\%} = 141 \text{ S cm}^{-1}$, confirming the plateau zone previously mentioned. Here, some saturation is occurring that is stable within $-1\% \geq \eta \geq -2\%$.

Surprisingly, a comparison between the AHC (in Fig. 3) and the states available near the Fermi level [see Fig. 2(g)] within the range $[-0.1, +0.1]$ eV, directly associated with $f_n(\vec{k})$, in Eq. (2), shows no correlation. Here, we expected to find a connection because of the $\Omega_\nu(\vec{k})$ dependence on the Fermi distribution. However, the number of states increases with the tension while the AHC gets almost destroyed under

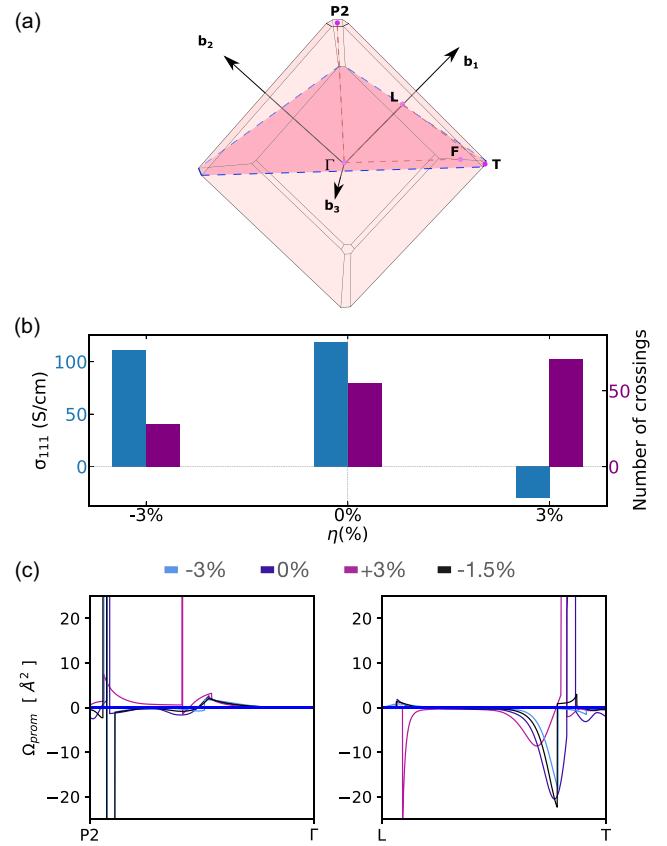


FIG. 4. (a) Brillouin zone for the rhombohedral structure of Mn_3NiN . Here, the plane parallel to the (111) plane is highlighted and the high symmetry points included in the band structure calculation. (b) Bar plot including the σ_{111} component of the AHC as well as the number of nontopological band crossings in the range $[-0.1, 0.1]$ eV around the Fermi level. (c) Berry curvature calculated for the path connecting the high symmetry points P2- Γ on the left and L-T on the right, perpendicular and parallel to the kagome lattices, respectively.

such circumstances. A DOS projection onto the Mn:3d and Ni:3d orbitals, which dominate most of the band structure around the Fermi level, showed a nonsimilar behavior to the AHC. The contribution of those orbitals follows the same rules as the total DOS, as already discussed in the electronic structure analysis. For instance, the only source of control that remains for the AHC is the Berry curvature, which will be analyzed in what follows. The Mn_3NiN BZ is shown in Fig. 4(a) in which P2- Γ and L-T are shown with respect to the (111) plane kagome lattice. In Fig. 4(b) is presented the AHC as well as the number of band crossings in the $[-0.1, 0.1]$ eV range. The BC integration results for $\eta = -3.0\%$, -1.5% , 0.0% , and 3.0% along the P2- Γ and the L-T paths are shown in the left and right parts of Fig. 4(c), respectively. Analyzing the BC along the P2- Γ path shown in Fig. 4(c), various discontinuities belonging to band crossings near and at the Fermi level can be identified. As provided by the symmetry analysis later in this paper, most of those crossings are not protected by the symmetries of the system and therefore belong to the nontopological band crossings classification. However, the rhombohedral symmetry preservation through-

out the strain application process is advantageous because it allows the shape of the band structure to remain mostly unaltered. As a result, the band crossings can only move up and down in energy or, in the case of nontopological band crossings, be dissolved by the external perturbation. Notably, the trivial band crossings near the Fermi level [shown in Figs. 2(a)–2(c)] produce a divergent component of the BC that is maximum for the unstrained structure, very weak for compression, but considerable for tension strain. Despite that, the results showed the highest AHC values for compression and unstrained cases, while in the case of tension strain, the AHC sees a minimum. Moreover, the counting of the band crossings near the Fermi energy shown in Fig. 4(b), in agreement with the DOS integral, shown in Fig. 2(g), displays a proportional compression (tension) to decrease (increase) of the number of crossings. Thus, giving more crossings near the Fermi level for tension than for compression and an intermediate number of crossings for the unstrained case. Again, the Berry curvature of the nontopological crossings does not follow the behavior already seen in the AHC. Therefore, in agreement with Huyen *et al.* [32], our results suggest that the highly localized and divergent Berry curvature, induced by the band crossings near the Fermi level, is not the AHC primary origin.

Despite several bands crossings found in the band structure, not all are actual Weyl nodes; instead, the majority are nontopological crossings, which resist small symmetry-preserving perturbations but do not result from the crystallographic and magnetic symmetries. In what follows, the Weyl nodes identification process will be presented.

Bands can be either spanned in Bloch or Wannier functions; the first unlocalized in the momentum space and the second localized in the real space. In this case, a relationship between the localized orbitals of atomic sites with the wave functions can be established [68,69]. Therefore, the crystal symmetry is inherited by the Hamiltonian. Thus, the reciprocal paths along where symmetry-protected Weyl nodes can be detected are determined from the character tables of the high symmetry points and the compatibility relations of the band representations for the symmetry group. The character tables and the compatibility relations were obtained from the Bilbao Crystallographic Server, providing information for all the known symmetry groups. Such tables are calculated through a generalized implementation of the induction algorithm based on the Frobenius reciprocity [70,71].

In systems like the Mn_3NiN Γ_{4g} magnetic phase, the degeneracy of the energy bands is lifted by the TRS breaking. However, some degeneracies remain due to their topological origin and are protected by nonsymmorphic symmetries (e.g., the roto-translations). According to the compatibility relations for the $R\bar{3}m'$ (166.101) magnetic symmetry group, the symmetries in this noncollinear antiferromagnet induce and the $C_{3(111)}$ protect a total of 6 possible Weyl nodes located along the path $\Gamma:(0,0,0) \rightarrow T:(1/2, 1/2, -1/2)$, each belonging to crossings of pairs of bands from the Γ point at an intermediate Λ point, which separates again towards the point T (see Table SIII in Supplemental Material [36]).

Because of the Weyl nodes protected status, they are resistant to all the symmetry-preserving perturbations in the system and are also nondependent on the SOC. Therefore, the

$C_{3(111)}$ protected Weyl nodes must hold against tiny or extreme strain values, such as $-3\% \leq \eta \leq +3\%$, either in the presence or the absence of the SOC. After analyzing the band structure in the T- Γ path for band degeneracies with band inversion, we identified some crossings that disappear under compression or tension, but four crossings hold from -3% to 3% strain (see Table SIV in Supplemental Material [36]). Among the found nodes, the Weyl node shown in Figs. 2(a)–2(c) occupying the energy levels -0.461 , -0.413 , and -0.4177 eV for -3% , 0% , and 3% , respectively, is the closest to the Fermi level. Despite remaining intact in all the strain cases, the mentioned crossing showed no inference in the BC at the Fermi level. Furthermore, as reported in Kübler *et al.* [72], the chirality of both, inward and outward magnetic moments triangles is the same, in which case the contribution of the Weyl nodes to the Berry curvature cancels out in pairs inside the AHC integral, Eq. (2). On the other hand, the BC in the L-T section, shown in Fig. 4(c), provides both types of BC, localized and not localized, over the path. The localized BC is once more uncorrelated to the AHC data. This confirms what has already been discussed in the BC analysis along the P2- Γ segment. Interestingly, the spread BC correlates to the AHC for each strain value. The highest values of the BC are $\Omega_{111}^{0\%} = -20.5 \text{ \AA}^2$, $\Omega_{111}^{-1.5\%} = -22.5 \text{ \AA}^2$, and $\Omega_{111}^{-3\%} = -18.4 \text{ \AA}^2$, while for $+3\%$ a relatively small value of BC is spotted $\Omega_{111}^{+3\%} = -8.6 \text{ \AA}^2$. The AHC values in each of the mentioned cases are $\sigma_{111}^{0\%} = 114 \text{ S cm}^{-1}$, $\sigma_{111}^{-1.5\%} = 140 \text{ S cm}^{-1}$, $\sigma_{111}^{-3\%} = 111 \text{ S cm}^{-1}$, and $\sigma_{111}^{+3\%} = -27 \text{ S cm}^{-1}$. It is important to remark that the L-T path lies in a plane parallel to the (111) plane, and the P2- Γ is parallel to the magnetic symmetry axis [i.e., along the (111) axis and perpendicular to the kagome lattice, see Fig. 4(a)]. Thus, as expected, the AHE occurs only over the (111) plane (i.e., into the kagome lattice) and not in the perpendicular direction. Therefore, the AHC, induced by a nonvanishing BC in the (111) plane, conducts the carriers over the same plane where the $\mathcal{T} * \mathcal{M}$ preserving magnetic orderings are placed. This nondivergent BC can be attributed to interband coherence induced by the electronic field [66]. Avoided band crossings at the Fermi energy level benefit the AHC due to the strong interaction of the occupied and the unoccupied bands [73–75]. The latter was observed for the computed BC within the (111) plane included in Fig. S3 in the Supplemental Material [36].

IV. CONCLUSIONS AND GENERAL REMARKS

Through first-principles calculations and theoretical analysis, we have investigated the strain-driven controlling of AHC in Mn_3NiN antiperovskite. We found that the strain application in the (111) plane preserves the symmetries of the system, allowing only control over the dispersion of the bands in energy. Such preservation keeps intact the source of the AHC, the $\mathcal{T} * \mathcal{M}$ in the Γ_{4g} magnetic ordering, leaving the AHC tensor form unchanged in each case. Therefore, the AHC is a function of the distance between the Mn atoms within the same and different kagome lattice planes. Our results indicate a nondirect relationship between the AHC magnitude and the epitaxial strain. Thus, compression (tension) strain values lead to an enhancing (decreasing) of

the AHC only within the range $-2\% \leq \eta \leq 1\%$ of strain. Moreover, we observed that the strain induced a redistribution of the AHC function maxima and minima near the Fermi energy. The magnitude of the AHC and the BC as strain functions showed a correlation over their components in the kagome lattice plane. However, there is a limit to this control mechanism. The maximum AHC value is reached between $-1\% \leq \eta \leq -2\%$; further compression only reduces the AHC. Remarkably, neither the total nor the $3d$ orbital projected DOS in the vicinity of the Fermi energy presented correlations to the AHC. Instead, the physics behind the tuning of the AHC relies on the nondivergent Berry curvature within the (111) kagome plane. Noteworthy, the AHC in this compound showed no correlation to the band crossings (trivial or topological), and the AHC could be traced to the avoided crossings and the interband coherences. The BC in the L–T path in this plane increases as the strain reduces the Mn–Mn distance. Therefore, the strain in the (111) plane proved to be an effective tool to tune the AHC in the Γ_{4g} magnetic phase of Mn_3NiN .

ACKNOWLEDGMENTS

We thank L. Flores-Gomez for helpful comments and discussions. Calculations presented in this paper were carried out using the GridUIS-2 experimental testbed, being

developed under the Universidad Industrial de Santander (SC3-UIS) High Performance and Scientific Computing Centre, development action with support from UIS Vicerrectoría de Investigación y Extensión (VIE-UIS) and several UIS research groups as well as other funding resources. The authors acknowledge the Texas Advanced Computing Center (TACC) at The University of Texas at Austin for providing (HPC, visualization, database, or grid). Additionally, we acknowledge the XSEDE facilities' support, a project from the National Science Foundation under Grant No. ACI-1053575. The authors also acknowledge the Texas Advanced Computer Center (with the Stampede2 and Bridges-2 supercomputers). We also acknowledge the use of the SuperComputing System (Thorny Flat) at WVU, which is funded in part by the National Science Foundation (NSF) Major Research Instrumentation Program (MRI) Award #1726534. A.C.G.C. acknowledges the Grant No. 2677: "Quiralidad y Ordenamiento Magnético en Sistemas Cristalinos: Estudio Teórico desde Primeros Principios" supported by the VIE-UIS. A.B.H acknowledges the computational support extended to us by Laboratorio de Supercomputo del Sureste (LNS), Benemérita Universidad Autónoma de Puebla, BUAP, for performing heavy theoretical calculations. The work by A.H.R. was supported by the Grant No. DE-SC0021375 funded by the U.S. Department of Energy, Office of Science.

-
- [1] S. V. Krivovichev, Minerals with antiperovskite structure: A review, *Z. Kristallogr.* **223**, 109 (2008).
 - [2] D. Boldrin, I. Samathrakris, J. Zemen, A. Mihai, B. Zou, F. Johnson, B. D. Esser, D. W. McComb, P. K. Petrov, H. Zhang, and L. F. Cohen, Anomalous Hall effect in noncollinear antiferromagnetic Mn_3NiN thin films, *Phys. Rev. Mater.* **3**, 094409 (2019).
 - [3] G. Gurung, D.-F. Shao, T. R. Paudel, and E. Y. Tsymlal, Anomalous Hall conductivity of noncollinear magnetic antiperovskites, *Phys. Rev. Mater.* **3**, 044409 (2019).
 - [4] T. Peng, W. Bo-Sen, and S. Yu-Ping, Mn-based antiperovskite functional materials: Review of research, *Chin. Phys. B* **22**, 067501 (2013).
 - [5] D. Boldrin, A. P. Mihai, B. Zou, J. Zemen, R. Thompson, E. Ware, B. V. Neamtu, L. Ghivelder, B. Esser, D. W. McComb *et al.*, Giant piezomagnetism in Mn_3NiN , *ACS Appl. Mater. Interfaces* **10**, 18863 (2018),.
 - [6] D. Fruchart and E. F. Bertaut, Magnetic studies of the metallic perovskite-type compounds of manganese, *J. Phys. Soc. Jpn.* **44**, 781 (1978)
 - [7] J. Zemen, E. Mendive-Tapia, Z. Gercsi, R. Banerjee, J. B. Staunton, and K. G. Sandeman, Frustrated magnetism and caloric effects in Mn-based antiperovskite nitrides: *Ab initio* theory, *Phys. Rev. B* **95**, 184438 (2017).
 - [8] Y. Wang, H. Zhang, J. Zhu, X. Lü, S. Li, R. Zou, and Y. Zhao, Antiperovskites with exceptional functionalities, *Adv. Mater.* **32**, 1905007 (2020).
 - [9] Y. Zhao and L. L. Daemen, Superionic conductivity in lithium-rich anti-perovskites, *J. Am. Chem. Soc.* **134**, 15042 (2012).
 - [10] K. Takenaka, T. Hamada, D. Kasugai, and N. Sugimoto, Tailoring thermal expansion in metal matrix composites blended by antiperovskite manganese nitrides exhibiting giant negative thermal expansion, *J. Appl. Phys.* **112**, 083517 (2012).
 - [11] A. C. Garcia-Castro, R. Ospina, and J. H. Quintero, Octahedral distortion and electronic properties of the antiperovskite oxide Ba_3SiO : First principles study, *J. Phys. Chem. Solids* **136**, 109126 (2020).
 - [12] A. C. Garcia-Castro, J. H. Quintero Orozco, and C. J. Paez Gonzalez, Hybrid-improper ferroelectric behavior in $\text{Ba}_3\text{SiO}/\text{Ba}_3\text{GeO}$ oxide antiperovskite superlattices, *Eur. Phys. J. B* **92**, 203 (2019).
 - [13] L. L. Boyer and P. J. Edwardson, Perovskite to antiperovskite in abf3 compounds, *Ferroelectrics* **104**, 417 (1990).
 - [14] P. Lukashev, R. F. Sabirianov, and K. Belashchenko, Theory of the piezomagnetic effect in Mn-based antiperovskites, *Phys. Rev. B* **78**, 184414 (2008).
 - [15] H. Liu and X. Yang, A brief review on perovskite multiferroics, *Ferroelectrics* **507**, 69 (2017).
 - [16] M. Fiebig, T. Lottermoser, D. Meier, and M. Trassin,, The evolution of multiferroics, *Nat. Rev. Mater.* **1**, 16046 (2016).
 - [17] N. A. Spaldin, S.-W. Cheong, and R. Ramesh, Multiferroics: Past, present, and future, *Phys. Today* **63**, 38 (2010).
 - [18] T. Wu, Z. Qin, Y. Wang, Y. Wu, W. Chen, S. Zhang, M. Cai, S. Dai, J. Zhang, J. Liu *et al.*, The main progress of perovskite solar cells in 2020-2021, *Nano-Micro Lett.* **13**, 152 (2021).
 - [19] J. Y. Kim, J.-W. Lee, H. S. Jung, H. Shin, and N.-G. Park, High-efficiency perovskite solar cells, *Chem. Rev.* **120**, 7867 (2020).
 - [20] T. Kasuya, A theory of metallic ferro- and antiferromagnetism on Zener's model, *Prog. Theor. Phys.* **16**, 45 (1956).

- [21] J. B. Goodenough, Theory of the role of covalence in the perovskite-type manganites [La, $m(\text{II})$]MnO₃, *Phys. Rev.* **100**, 564 (1955).
- [22] J. Kanamori, Superexchange interaction and symmetry properties of electron orbitals, *J. Phys. Chem. Solids* **10**, 87 (1959).
- [23] K. Matan, B. M. Bartlett, J. S. Helton, V. Sikolenko, S. Mat'áš, K. Prokeš, Y. Chen, J. W. Lynn, D. Grohol, T. J. Sato, M. Tokunaga, D. G. Nocera, and Y. S. Lee, Dzyaloshinskii-Moriya interaction and spin reorientation transition in the frustrated kagome lattice antiferromagnet, *Phys. Rev. B* **83**, 214406 (2011).
- [24] D. Grohol, K. Matan, J.-H. Cho, S.-H. Lee, J. W. Lynn, D. G. Nocera, and Y. S. Lee, Spin chirality on a two-dimensional frustrated lattice, *Nat. Mater.* **4**, 323 (2005).
- [25] T. Hikihara, L. Kecke, T. Momoi, and A. Furusaki, Vector chiral and multipolar orders in the spin- $\frac{1}{2}$ frustrated ferromagnetic chain in magnetic field, *Phys. Rev. B* **78**, 144404 (2008).
- [26] L. Šmejkal, Y. Mokrousov, B. Yan, and A. H. MacDonald, Topological antiferromagnetic spintronics, *Nat. Phys.* **14**, 242 (2018).
- [27] N. Kiyohara, T. Tomita, and S. Nakatsuji, Giant anomalous Hall effect in the chiral antiferromagnet Mn₃Ge, *Phys. Rev. Appl.* **5**, 064009 (2016).
- [28] S. Nakatsuji, N. Kiyohara, and T. Higo, Large anomalous Hall effect in a non-collinear antiferromagnet at room temperature, *Nature (London)* **527**, 212 (2015).
- [29] A. K. Nayak, J. E. Fischer, Y. Sun, B. Yan, J. Karel, A. C. Komarek, C. Shekhar, N. Kumar, W. Schnelle, J. Kübler, C. Felser, and S. S. P. Parkin, Large anomalous Hall effect driven by a nonvanishing berry curvature in the noncollinear antiferromagnet Mn₃Ge, *Sci. Adv.* **2**, e1501870 (2016).
- [30] A. Pulkkinen, B. Barbiellini, J. Nokelainen, V. Sokolovskiy, D. Baigutlin, O. Miroshkina, M. Zagrebin, V. Buchelnikov, C. Lane, R. S. Markiewicz, A. Bansil, J. Sun, K. Pussi, and E. Lähderanta, Coulomb correlation in noncollinear antiferromagnetic α -Mn, *Phys. Rev. B* **101**, 075115 (2020).
- [31] D. Hobbs, J. Hafner, and D. Spišák, Understanding the complex metallic element Mn. I. Crystalline and noncollinear magnetic structure of α -Mn, *Phys. Rev. B* **68**, 014407 (2003).
- [32] Vu Thi Ngoc Huyen, M.-T. Suzuki, K. Yamauchi, and T. Oguchi, Topology analysis for anomalous Hall effect in the non-collinear antiferromagnetic states of Mn₃AN ($a = \text{Ni, Cu, Zn, Ga, Ge, Pd, In, Sn, Ir, Pt}$), *Phys. Rev. B* **100**, 094426 (2019).
- [33] D. Boldrin, F. Johnson, R. Thompson, A. P. Mihai, B. Zou, J. Zemen, J. Griffiths, P. Gubeljak, K. L. Ormandy, P. Manuel *et al.*, The biaxial strain dependence of magnetic order in spin frustrated Mn₃NiN thin films, *Adv. Funct. Mater.* **29**, 1902502 (2019).
- [34] X. Zhou, J.-P. Hanke, W. Feng, F. Li, G.-Y. Guo, Y. Yao, S. Blügel, and Y. Mokrousov, Spin-order dependent anomalous Hall effect and magneto-optical effect in the noncollinear antiferromagnets Mn₃xN with $x = \text{Ga, Zn, Ag, or Ni}$, *Phys. Rev. B* **99**, 104428 (2019).
- [35] K. Zhao, T. Hajiri, H. Chen, R. Miki, H. Asano, and P. Gegenwart, Anomalous Hall effect in the noncollinear antiferromagnetic antiperovskite Mn₃Ni_{1-x}Cu_xN, *Phys. Rev. B* **100**, 045109 (2019).
- [36] See Supplemental Material at <http://link.aps.org/supplemental/10.1103/PhysRevB.106.195113> for further details on the structural stability, the optimization, the Berry curvature and the Weyl nodes in Mn₃NiN.
- [37] C. X. Quintela, K. Song, D.-F. Shao, L. Xie, T. Nan, T. R. Paudel, N. Campbell, X. Pan, T. Tybell, M. S. Rzechowski *et al.*, Epitaxial antiperovskite/perovskite heterostructures for materials design, *Sci. Adv.* **6**, eaba4017 (2020).
- [38] C. X. Quintela, N. Campbell, D. F. Shao, J. Irwin, D. T. Harris, L. Xie, T. J. Anderson, N. Reiser, X. Q. Pan, E. Y. Tsymlal *et al.*, Epitaxial thin films of Dirac semimetal antiperovskite Cu₃PdN, *APL Mater.* **5**, 096103 (2017).
- [39] F. Johnson, D. Boldrin, J. Zemen, D. Pesquera, J. Kim, X. Moya, H. Zhang, H. K. Singh, I. Samathrakakis, and L. F. Cohen, Strain dependence of Berry-phase-induced anomalous Hall effect in the non-collinear antiferromagnet Mn₃NiN, *Appl. Phys. Lett.* **119**, 222401 (2021).
- [40] P. Hohenberg and W. Kohn, Inhomogeneous electron gas, *Phys. Rev.* **136**, B864 (1964).
- [41] W. Kohn and L. J. Sham, Self-consistent equations including exchange and correlation effects, *Phys. Rev.* **140**, A1133 (1965).
- [42] G. Kresse and J. Furthmüller, Efficient iterative schemes for *ab initio* total-energy calculations using a plane-wave basis set, *Phys. Rev. B* **54**, 11169 (1996).
- [43] G. Kresse and D. Joubert, From ultrasoft pseudopotentials to the projector augmented-wave method, *Phys. Rev. B* **59**, 1758 (1999).
- [44] P. E. Blöchl, Projector augmented-wave method, *Phys. Rev. B* **50**, 17953 (1994).
- [45] J. P. Perdew, A. Ruzsinszky, G. I. Csonka, O. A. Vydrov, G. E. Scuseria, L. A. Constantin, X. Zhou, and K. Burke, Restoring the Density-Gradient Expansion for Exchange in Solids and Surfaces, *Phys. Rev. Lett.* **100**, 136406 (2008).
- [46] A. I. Liechtenstein, V. I. Anisimov, and J. Zaanen, Density-functional theory and strong interactions: Orbital ordering in Mott-Hubbard insulators, *Phys. Rev. B* **52**, R5467 (1995).
- [47] H. K. Singh, I. Samathrakakis, N. M. Fortunato, J. Zemen, C. Shen, O. Gutfleisch, and H. Zhang, Multifunctional antiperovskites driven by strong magnetostructural coupling, *npj Comput. Mater.* **7**, 98 (2021).
- [48] J. Sun, A. Ruzsinszky, and J. P. Perdew, Strongly Constrained and Appropriately Normed Semilocal Density Functional, *Phys. Rev. Lett.* **115**, 036402 (2015).
- [49] L. Florez-Gomez, W. Ibarra-Hernandez, and A. C. Garcia-Castro, Exploration of the spin-phonon coupling in the non-collinear antiferromagnetic antiperovskite Mn₃NiN, *J. Magn. Magn. Mater.* **562**, 169813 (2022).
- [50] G. Sai Gautam and E. A. Carter, Evaluating transition metal oxides within DFT-SCAN and SCAN + U frameworks for solar thermochemical applications, *Phys. Rev. Mater.* **2**, 095401 (2018).
- [51] I. G. Buda, C. Lane, B. Barbiellini, A. Ruzsinszky, J. Sun, and A. Bansil, Characterization of thin film materials using SCAN meta-GGA, an accurate nonempirical density functional, *Sci. Rep.* **7**, 44766 (2017).
- [52] B. Barbiellini, A. Pulkkinen, J. Nokelainen, V. Buchelnikov, V. Sokolovskiy, O. N. Miroshkina, M. Zagrebin, K. Pussi, E. Lähderanta, and A. Granovsky, Correlation effects in the ground state of Ni-(Co)-Mn-Sn Heusler compounds, *MRS Adv.* **4**, 441 (2019).

- [53] H. J. Monkhorst and J. D. Pack, Special points for Brillouin-zone integrations, *Phys. Rev. B* **13**, 5188 (1976).
- [54] D. Hobbs, G. Kresse, and J. Hafner, Fully unconstrained noncollinear magnetism within the projector augmented-wave method, *Phys. Rev. B* **62**, 11556 (2000).
- [55] S. S. Tsirkin, High performance Wannier interpolation of Berry curvature and related quantities with WannierBerri code, *npj Comput. Mater.* **7**, 33 (2021).
- [56] G. Pizzi, V. Vitale, R. Arita, S. Blügel, F. Freimuth, G. Géranton, M. Gibertini, D. Gresch, C. Johnson, T. Koretsune *et al.*, Wannier90 as a community code: New features and applications, *J. Phys.: Condens. Matter* **32**, 165902 (2020).
- [57] Q. Wu, S. Zhang, H.-F. Song, M. Troyer, and A. A. Soluyanov, Wanniertools: An open-source software package for novel topological materials, *Comput. Phys. Commun.* **224**, 405 (2018).
- [58] K. Momma and F. Izumi, *VESTA3* for three-dimensional visualization of crystal, volumetric and morphology data, *J. Appl. Cryst.* **44**, 1272 (2011).
- [59] U. Herath, P. Tavazde, X. He, E. Bousquet, S. Singh, F. Muñoz, and A. H. Romero, Pyprocar: A python library for electronic structure pre/post-processing, *Comput. Phys. Commun.* **251**, 107080 (2020).
- [60] Y. Na, C. Wang, L. Chu, L. Ding, J. Yan, Y. Xue, W. Xie, and X. Chen, Preparation and properties of antiperovskite Mn_3NiN thin film, *Mater. Lett.* **65**, 3447 (2011).
- [61] E. Bertaut and D. Fruchart, Rotation des moments magnetiques du manganese DANS Mn_3NiN , *Intern. J. Magn.* **2**, 259 (1972).
- [62] D. Fruchart, E. F. Bertaut, J. P. Sénateur, and R. Fruchart, Magnetic studies on the metallic perovskite-type compound Mn_3SnN , *J. Phys. Lett.* **38**, 21 (1977).
- [63] M. Mochizuki, M. Kobayashi, R. Okabe, and D. Yamamoto, Spin model for nontrivial types of magnetic order in inverse-perovskite antiferromagnets, *Phys. Rev. B* **97**, 060401(R) (2018).
- [64] H. T. Stokes and D. M. Hatch, *FINDSYM*: Program for identifying the space-group symmetry of a crystal, *J. Appl. Cryst.* **38**, 237 (2005).
- [65] H. Stokes, D. Hatch, and B. Campbell, Findsymb, ISOTROPY Software Suite, iso. byu. edu (2017).
- [66] N. Nagaosa, J. Sinova, S. Onoda, A. H. MacDonald, and N. P. Ong, Anomalous Hall effect, *Rev. Mod. Phys.* **82**, 1539 (2010).
- [67] M. Seemann, D. Ködderitzsch, S. Wimmer, and H. Ebert, Symmetry-imposed shape of linear response tensors, *Phys. Rev. B* **92**, 155138 (2015).
- [68] J. Zak, Symmetry Specification of Bands in Solids, *Phys. Rev. Lett.* **45**, 1025 (1980).
- [69] J. Zak, Band representations and symmetry types of bands in solids, *Phys. Rev. B* **23**, 2824 (1981).
- [70] B. Bradlyn, L. Elcoro, J. Cano, M. G. Vergniory, Z. Wang, C. Felser, M. I. Aroyo, and B. A. Bernevig, Topological quantum chemistry, *Nature (London)* **547**, 298 (2017).
- [71] M. I. Aroyo, A. Kirov, C. Capillas, J. M. Perez-Mato, and H. Wondratschek, Bilbao crystallographic server. II. Representations of crystallographic point groups and space groups, *Acta Cryst. A* **62**, 115 (2006).
- [72] J. Kübler and C. Felser, Non-collinear antiferromagnets and the anomalous Hall effect, *Europhys. Lett.* **108**, 67001 (2014).
- [73] X. Wang, J. R. Yates, I. Souza, and D. Vanderbilt, *Ab initio* calculation of the anomalous Hall conductivity by Wannier interpolation, *Phys. Rev. B* **74**, 195118 (2006).
- [74] X. Wang, D. Vanderbilt, J. R. Yates, and I. Souza, Fermi-surface calculation of the anomalous Hall conductivity, *Phys. Rev. B* **76**, 195109 (2007).
- [75] Y. Yao, L. Kleinman, A. H. MacDonald, J. Sinova, T. Jungwirth, D.-s. Wang, E. Wang, and Q. Niu, First Principles Calculation of Anomalous Hall Conductivity in Ferromagnetic bcc Fe, *Phys. Rev. Lett.* **92**, 037204 (2004).